Discovering the Influence of Lithium Loss on Garnet $Li_7La_3Zr_2O_{12}$ Electrolyte Phase Stability

Andrea Paolella, Wen Zhu, Giovanni Bertoni, Sylvio Savoie, Zimin Feng, Hendrix Demers, Vincent Gariepy, Gabriel Girard, Etienne Rivard, Nicolas Delaporte, Abdelbast Guerfi, Henning Lorrmann, Chandramohan George, and Karim Zaghib*

Introduction

Post-Li ion technologies such as Li metal, Li–S, and Li–O_2 batteries are gaining traction because of their very high energy density. However, Li metal batteries inherently suffer from the problem of Li dendrites which can cause safety hazards due to battery short circuiting in the presence of flammable organic liquid electrolyte, (1–3) and in Li–S and Li–O_2 batteries, electrode particles dissolution and electrolyte decomposition are recurrent issues that drastically limit their electrochemical performance and round-trip efficiencies. Considerable effort has been dedicated to develop solid electrolytes such as polymers (PEO-LiTFSI), (4,5) ceramics (e.g., garnet (6) and LiPON (7)), and hybrid electrolytes (e.g., ceramics dispersed in PEO:LiTFSI), (8,9) for all-solid-state Li metal, Li–S, and Li–O_2 batteries, where these solid electrolytes are expected to alleviate the above deleterious processes and thereby improve battery safety, energy density, and longevity. However, each of these electrolytes requires a trade-off between their properties and actual electrochemical requirements. For example, polymer electrolytes based on standard poly(ethylene oxide) (PEO) and LiTFSI salt not only have low conductivity (~10^{-5} S/cm at room temperature) but tend to decompose above 4.0 V. (10) Similarly, the addition of ceramics (Al_2O_3 or SiO_2) into polymer matrixes has been shown to increase the total ionic conductivity (lattice and grain boundary) to some extent, but high voltage stability is still required. The addition of ionic conductor fillers ($Li_7La_3Zr_2O_{12}$) in hybrid ceramic–polymer electrolyte can cause some decomposition reactions of garnet as reported by Zheng et al. (11) In the category of inorganic electrolytes, thio-glasses (12,13) were synthesized via reacting mixtures of Li_2S, P_2S_5, and metal sulfides such as GeS_2, SiS_2, and SnS_2 at low temperatures. They are good ionic conductors (up to 10^{-3} S/cm), but they suffer from moisture contamination (forming H_2S and LiOH) and have narrow electrochemical stability window (1.0–2.8 V) that cause decomposition reactions at both electrodes. (14,15) Following studies on antiperovskites (Li_3OCl and Li_3OBr), (16) new glass electrolytes (17) based on LiOH, $Ba(OH)_2$, and LiCl with interesting electrochemical properties were recently proposed, which rely on multistep fabrication. (18) Unfortunately a lithium–proton ion exchange presents difficulties in distinguishing

between Li_3OCl and Li_2OHCl as reported by Hanghofer et al. (19) Although phosphate-based electrolytes such as $Li_{1.5}Al_{0.5}Ge_{1.5}(PO_4)_3$ (LAGP) (20) and $Li_{1.5}Al_{0.5}Ti_{1.5}(PO_4)_3$ (LATP) (21) appear to be good ionic conductors ($\sim 10^{-4}$ S/cm), their poor chemical stability when in contact with lithium is a concern as indicated by Chung et al. (22)

Considering all the aspects discussed above, the $Li_7La_3Zr_2O_{12}$ (LLZO)-based garnet has emerged as a promising solid electrolyte mainly due to its high thermodynamic voltage stability (up to 5 V vs Li^+/Li), and good compatibility with negative electrodes. (23) LLZO exists in the two known polymorphs: tetragonal LLZO (t-LLZO) and cubic LLZO (c-LLZO). (24) LLZO is typically synthesized through a solid-state reaction (SSR) by mixing a lithium precursor (mainly lithium hydroxide or carbonate), lanthanum precursor (mainly lanthanum hydroxide or oxide), and zirconium precursor (mainly zirconium oxide or isopropoxide). In general, undoped LLZO has readily been synthesized only in a tetragonal phase, which possesses a much lower ionic conductivity compared to its other polymorph, the cubic phase LLZO. On the other hand, c-LLZO can be obtained only when the additional dopants such as iron, (25) gallium, (26–28) aluminum, (29–31) tantalum, (32) and niobium (33) are supplied alongside the base LLZO precursors. Concerning the role of dopants in the synthesis of c-LLZO, some theoretical studies (34) proposed that dopants play a role in stabilizing the cubic phase at room temperature and in increasing c-LLZO's ionic conductivity and in substituting for Li in Li sites. Kubicek et al. (35) have shown the importance of oxygen vacancies in Ga- and Ta-doped c-LLZO. Some studies have also reported the synthesis of undoped c-LLZO at low temperature: Xie et al. (36) have shown a low-temperature LLZO phase (700 °C) obtained via annealing acetate-based precursors, which exhibited a low ionic conductivity on the order of 10^{-6} S cm^{-1}. In 2013, Larraz et al. (37) demonstrated that it is possible to stabilize cubic structure at low temperature by proton exchange forming a low-temperature c-LLZO but with a very low ionic conductivity. In 2015, Yang et al. (38) reported a synthesis of undoped c-LLZO by the electrospinning method (with no details on ionic conductivity). In 2018, Weller et al. (39) reported a synthesis of undoped c-LLZO via molten salt method, but its ionic conductivity was not reported. It is therefore crucial to gain a comprehensive understanding of how LLZO chemical phase and composition evolved during SSR that suffers from heavy Li loss via volatilization and how such Li loss can be controlled directly during SSR to achieve the phase stability, high ionic conductivity, and chemical stability conducive to the development of all-solid-state batteries. More importantly, although low-temperature c-LLZO (undoped) is appealing, their conductivities are not suitable for battery applications. In this work, we deepened the investigation into chemical phase behavior of LLZO under various SSR conditions, and the samples produced at different stages of SSR were analyzed via *in situ* XRD for LLZO phase evolution, and the final products obtained were then analyzed via high-resolution HRTEM-EELS-EDX including chemical mapping and quantification for LLZO composition. We show that c-LLZO (with phase stability and good ionic conductivities) can be

prepared without needing additional dopants, as this can be achieved by regulating the decomposition of lithium carbonate precursor that appears to control Li loss during the SSR. In doing so, we found that an additional role of dopants in a typical SSR yielding c-LLZO is to control the lithium carbonate decomposition rate, which in turn allows for the control of Li loss or results in more accessible Li, leading to the formation of cubic phase LLZO, besides they improve ionic conductivity and stabilize lithium dynamics in the electrolyte. The findings from our mechanistic studies into the synthesis of c-LLZO via SSR can incentivize new research in the design and manufacturing of garnet-type solid electrolytes with optimized properties for developing all-solid-state energy storage.

Results and Discussion

Phase Stability of Undoped LLZO with a Cubic Structure (c-LLZO) and Role of Dopants

The precursors used for preparing undoped LLZO are detailed in the Methods section (see the Supporting Information). In a typical SSR, the ball-milled (LLZO precursors) powder was loaded onto a crucible (graphite boat), annealed at 700 °C for 2 h to remove water and adsorbed species (e.g., CO_2 from La_2O_3), (40) and subsequently heated at 950 °C for 2 h. We used graphite crucibles as the commonly used aluminum crucibles can cause contamination due to Al doping. With a constant flow of N_2 gas throughout the heating process, we observed the formation of standard tetragonal LLZO (Figure 1a,c,e). On the contrary, when the N_2 flow was stopped at the end of the annealing at 700 °C and subsequent heating process at 950 °C (no gas flow), we observed the formation of cubic LLZO after cooling to room temperature (Figure 1b,d,f), and this product was found to be stable (without undergoing any further phase change), which is rather surprising because the formation of cubic LLZO typically needs the presence of additional dopants acting as phase stabilizing agent; this represents the first undoped solid-state synthesis using Li_2CO_3, La_2O_3, and ZrO_2 precursors. We also remark that if this cubic LLZO phase exhibits higher conductivity than the low-temperature cubic LLZO (undoped) reported previously, this holds new promise for the process of high quality garnet electrolytes. These experiments show that gas flow can in fact dictate the final phase of LLZO in the SSR.

Figure 1

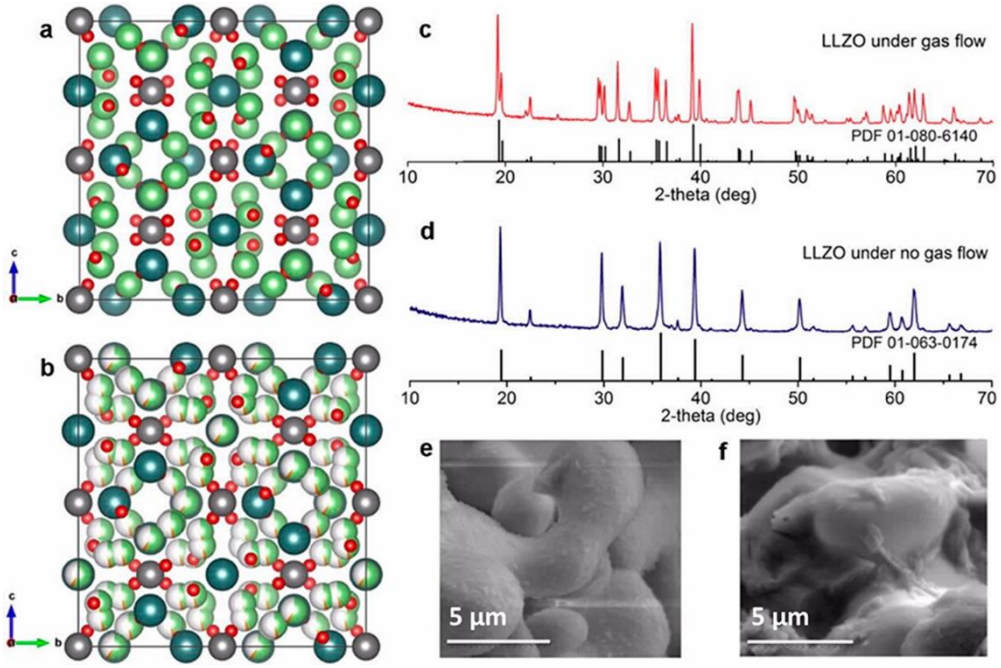

Figure 1. Crystal structures projected along the [100] direction with similar $Li_7La_3Zr_2O_{12}$ (LLZO) stoichiometry and (a) tetragonal structure; (b) cubic-LLZO. In the sketches, La is dark green, Zr is gray, and O is red. In the cubic structure more positions for Li atoms (light green) with partial occupancy are allowed. In the tetragonal structure, Li atoms sites have full occupancy, and in the case of Ga-doped LLZO, some of the Li atoms are substituted by Ga (orange segment at the Li sites). XRD diffraction patterns of the samples obtained at different conditions: (c) annealed at 950 °C with N_2 gas flow; (d) annealed without gas flow at 700 °C. SEM secondary electron image (the scale bar is 2 µm) of (e) LLZO obtained with gas flow and (f) LLZO without gas flow.

To understand how the gas flow (N_2) influences the phase evolution in LLZO, we performed *in situ* X-ray diffraction (XRD) analysis of the samples obtained by heating LLZO precursors under four different conditions: (i) with N_2 gas flow, (ii) no N_2 gas flow at T > 700 °C, (iii) with N_2 gas flow but with Ga as a dopant, and (iv) under vacuum. Under the constant N_2 flow, Figure 2a–c shows the XRD spectra at the beginning (a) and end (b) of the heat treatment at 850 °C as well as at room temperature after cooling (c). When the temperature reached 850 °C, the main phase formed was cubic-LLZO (PDF: 00-063-0174, in black), and the amount of this cubic-LLZO increased over time until the end of the heat treatment and then started undergoing a phase transition from cubic to tetragonal LLZO during cooling step.

Figure 2

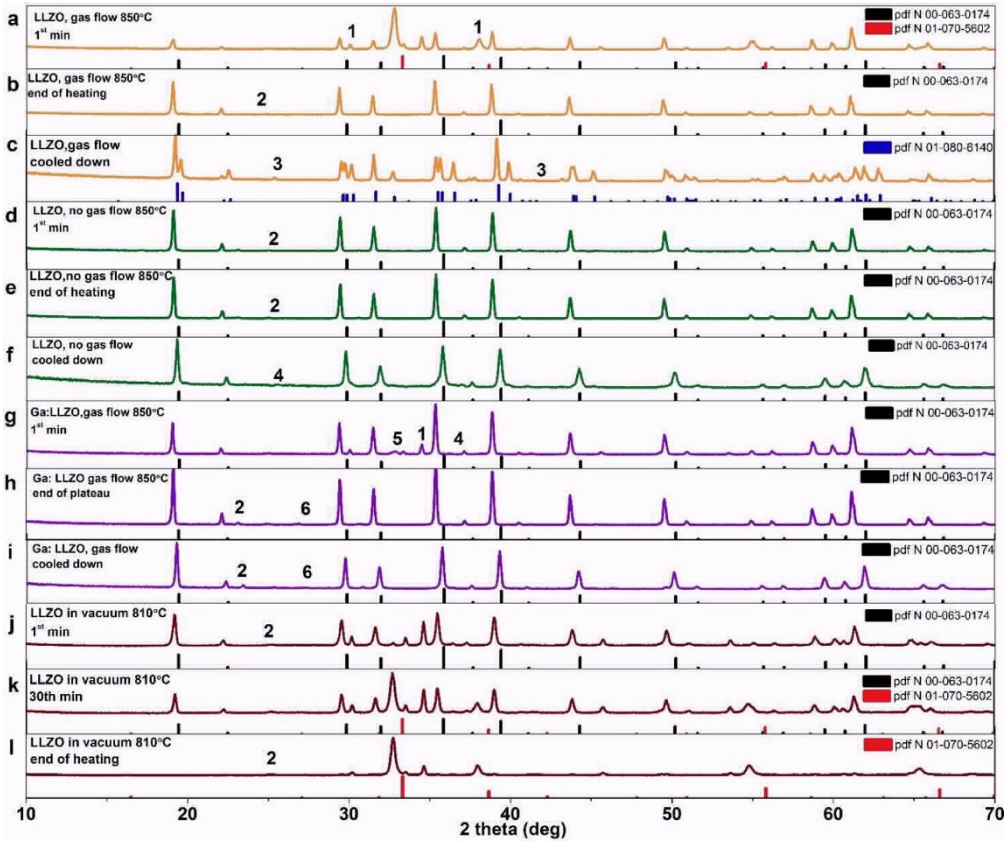

Figure 2. Comparison of *in situ* XRD diffraction patterns of different samples annealed at 850 °C and cooled for (a–c) undoped LLZO with N_2 gas flow, (d–f) undoped LLZO without N_2 gas flow, (g–i) Ga-doped LLZO with N_2 gas flow, and (j–l) undoped LLZO under vacuum. Some impurities are present: in the graphs, La_2O_3 is marked with 1, Li_2ZrO_3 is marked with 2, Li_8ZrO_6 is marked with 3, ZrO_2 is marked with 4, $La_2Zr_2O_7$ is marked with 5, and Li_5GaO_4 is marked with 6.

It can be noticed (PDF: 01-080-6140, in blue) that the cubic-LLZO had disappeared at the end of the cooling step, as it was turned into almost a single LLZO tetragonal phase in the final sample. On the other hand, Figure 2d–f (no N_2 gas flow at T >700 °C) shows that mostly the LLZO cubic structure was obtained at beginning of the synthesis, which was also preserved even after cooling. This result is similar to the case where the synthesis was performed under N_2 gas flow but with gallium (Ga) as dopant acting as a phase stabilizer, shown in Figure 2g–i. In fact, the LLZOs spectral features from both samples are almost overlapped (Figure S1 in the Supporting Information), which, in turn, suggests the crystal structure of undoped LLZO obtained from our gas flow stop method is basically the same as that of the Ga-LLZO (via doping route). These experiments in combination (Figure 2a–i) show that either cutting the N_2 flow or under N_2 flow with a dopant leads to the same result, that is, the formation of cubic-LLZO in a stable form not only at the high temperature but at room temperature. Lastly, in the synthesis performed under vacuum, some cubic-LLZO was formed at the beginning of the heat treatment at 810 °C, but it disappeared within ~150 min, leaving behind

$La_2Zr_2O_7$ (PDF card number 01-070-5602, marked with red) as a main compound together with a small amount of La_2O_3, indicating that a complete loss of Li either from initially formed LLZO or discontinued availability of Li suppressing the LLZO formation as shown in Figure 2j–l, which is in agreement with the study of Huang et al. (41) From the above experiments, it can be deduced that the formation of stable cubic phase LLZO can be related to Li availability, which should then depend on the decomposition kinetics of Li_2CO_3 because a) it either can supply Li in an easy accessible form, such as liquid, for fast c-LLZO formation or b) quickly decomposes to make Li inaccessible (e.g., Li_2O). We think that Li_2O becomes inaccessible because it precipitates out, and based on its melting point it can fast react only at temperatures higher than 950–1000 °C (1438 °C). Several lithium salts can be used as lithium source such as Li_2CO_3, LiOH, $LiNO_3$, and CH_3COOLi, but Li_2O is not a preferred choice as Li precursor directly because of its high melting point (especially in high temperature solid-state process). In synthesis, the lithium salts tend to decompose, forming gas species such as CO_2, N_2O_4, and H_2O, and the reaction between lithium salt and $La_2Zr_2O_7$ and La_2O_3 forming $Li_7La_3Zr_2O_{12}$ further accelerates the gaseous species to be formed. (42) As Li_2CO_3 starts to decompose partially at 740 °C, it becomes amorphous and liquid (molten state) in equilibrium with CO_2 gas, which is in agreement with the previous *in situ* observations. (42,43) Then, as the decomposition of Li_2CO_3 continues, it becomes dependent on the extent of degassing and effective removal of CO_2 (44) that is produced. This step seems to result either in the formation of Li_2O (in agreement with the work by Chen et al. (42)) that is inaccessible or in LLZO when molten Li_2CO_3 is in contact with $La_2Zr_2O_7$ and La_2O_3.

From the *in situ* XRD measurements (Figure 2), it can be concluded that $La_2Zr_2O_7$ is formed first, at which stage Li availability is a key parameter to complete the reaction leading to cubic-LLZO. In other words, CO_2 must be released upon only completing the final step that yields LLZO with right stoichiometry and if CO_2 is released earlier, this means most of Li become inaccessible to the final step of reaction producing LLZO. Therefore, the reaction involving Li_2CO_3 and $La_2Zr_2O_7$ can be written as follows in eq 1:

$$7Li_2CO_3 + La_2O_3 + 2La_2Zr_2O_7 \rightarrow 2Li_7La_3Zr_2O_{12} + 7CO_2 \quad \textbf{(1)}$$

In general, the formation of $La_2Zr_2O_7$ in solid-state synthesis of LLZO (45) was often reported, which can be explained by considering the decomposition of lithium carbonate in the same way that leads to Li inaccessibility or loss (e.g., via Li_2O formation in agreement with Chen et al. (42)), triggering the formation of off-stoichiometric LLZO compounds and impurities. For example, the undoped c-LLZO reported by Xie et al. (36) showed a very low total ionic conductivity at room temperature ($\sim 2 \times 10^{-6}$ S/cm), which was obtained at low temperature (700 °C), and with increasing synthesis temperature much more $La_2Zr_2O_7$ was formed due to lithium loss, which is in line with our observation of the metastability of undoped cubic-LLZO under the gas flow condition. To see how this Li loss is

influenced by the presence of a dopant, we performed more synthesis under gas flow with Ga dopants (Figure 2g–i), which invariably yielded cubic-LLZO as the main compound and Li_8ZrO_6 and Li_5GaO_4 as minor phases. All *in situ* XRD patterns collected during the SSR are summarized in the Supporting Information (Figures S2–S5). Figure 3 shows the high-resolution transmission electron microscopy (HRTEM) image and scanning transmission electron microscopy and energy-dispersive X-ray (STEM-EDXS) mapping of gallium-doped LLZO particles after synthesis. It can be noted that Ga distribution is homogeneous throughout the LLZO crystal with the presence of some gallium-enriched domains, presumably due to Li_5GaO_4 based on their XRD patterns.

Figure 3

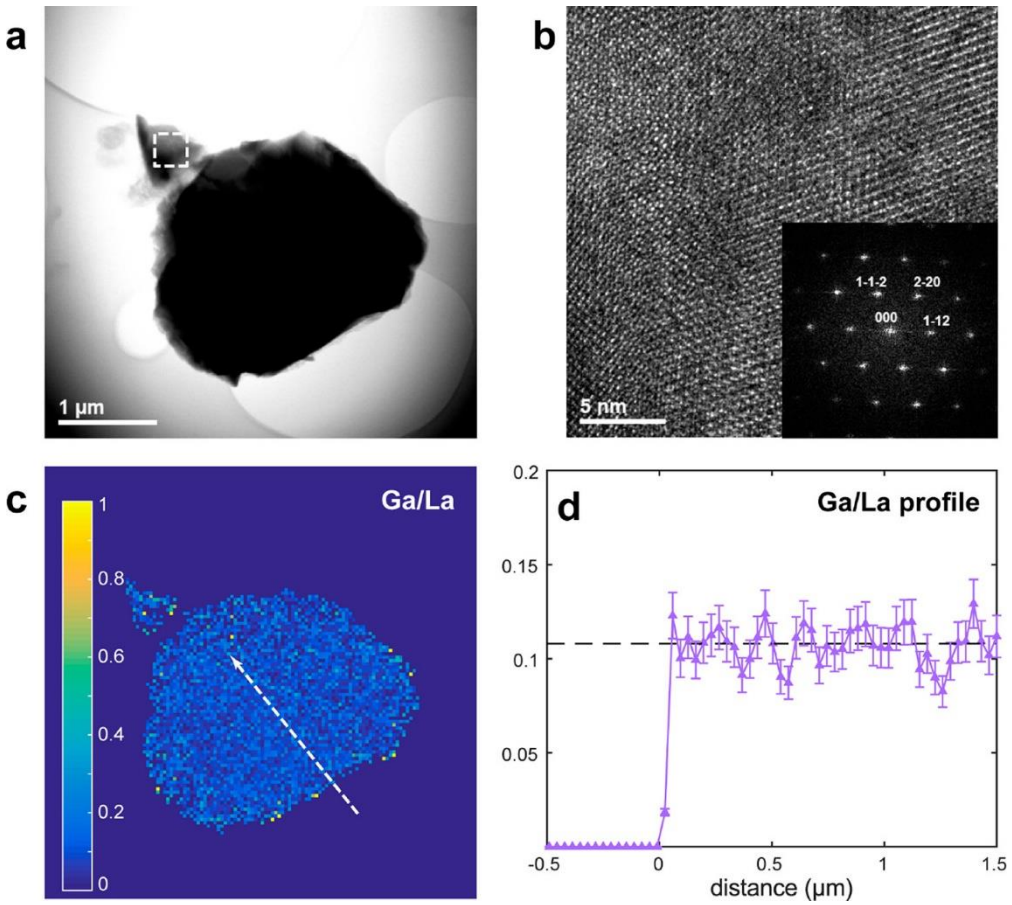

Figure 3. Transmission electron microscopy images and STEM-EDXS chemical mapping of Ga-doped LLZO. (a) BF-STEM image of a Ga-LLZO crystal. (b) HRTEM showing a [110] orientation from the region indicated in (a) with a square. (c) Ga/La ratio resulting from STEM-EDXS mapping from the crystal in (a). (d) Profile of the ratio along the direction indicated in (c). An error bar of 10% was considered in the ratio. The dashed line is the average ratio in the bulk of the crystal.

This indicates that the substitution of Ga dopants during LLZO phase evolution appears to help retain Li (from Li_2CO_3 decomposition before turning into inaccessible Li_2O), which in turn stabilizes the cubic-LLZO phase. In fact, it was reported that segregation of dopants at grain boundaries after pellet sintering at high temperature, which can explain how dopants preserve lithium loss as reported

by El Shinawi et al. (26) In our case, the observation of cubic-LLZO structure at high temperature backs up the proposed mechanism. This is further reflected in the fact that higher surface lithium concentration in the cubic-LLZO, and high overall Li concentration in the Ga-doped LLZO is found compared to undoped tetragonal LLZO, as shown by STEM-EELS in Figure 4. This means that severe Li loss during LLZO phase evolution leads to tetragonal phase. All the three samples (undoped cubic-LLZO, undoped tetragonal LLZO and Ga:LLZO) that were synthesized have the same La_2Zr_2O7 intermediate before cooling down, and cubic-LLZO is a well-known intermediate at high temperature (Figure S6). Therefore, considering the fact that cubic-LLZO is converted into tetragonal LLZO under gas flow, it it can be reasonably argued that the only difference between room temperature tetragonal LLZO and cubic-LLZO is the relative loss of lithium. This is reflective of the fact that when $La_2Zr_2O_7$ is formed, it needs to react with molten Li_2CO_3 to form the initial cubic-LLZO phase needing continuous supply of Li in surplus to stabilize the structure. If lithium is unavailable (equal to the amount of Li_2CO_3 that decomposes too quickly and becomes inaccessible Li_2O), the high-temperature garnet cubic-LLZO is then slowly converted into the tetragonal phase during cooldown. It therefore turns out that with a lithium deficiency cubic-LLZO is the most stable phase at high temperature, while tetragonal LLZO is the most stable phase at room temperature. The lattice parameters *a* obtained are 13.002 and 12.991 Å for undoped and Ga-doped LLZO, respectively, with the relative difference of 0.00085, further confirm (Figure S1) that both the undoped LLZO obtained under no gas flow and the Ga-LLZO have the same crystal structures. Because we prepared a ~4 g batch of undoped LLZO powder to perform all the experiments with and without gas flow (Figure S6), we can absolutely exclude that undoped cubic-LLZO is the result of accidental doping or cross-contamination, and no dopants were observed by EDS (see the Supporting Information) as the synthesis was performed on graphite crucibles. Further analysis could be performed, for example, ICP-based quantification, but such bulk lithium quantification is not useful here because both tetragonal and undoped cubic-LLZO will have the same content of lithium before and after synthesis. Because of this, EELS seems to be the only method to directly understand lithium dynamics on crystals. More details on the EELS quantification procedure, atomic ratio determination, ADF-STEM survey image for particles, and EELS signal extraction are presented in the Supporting Information.

Figure 4

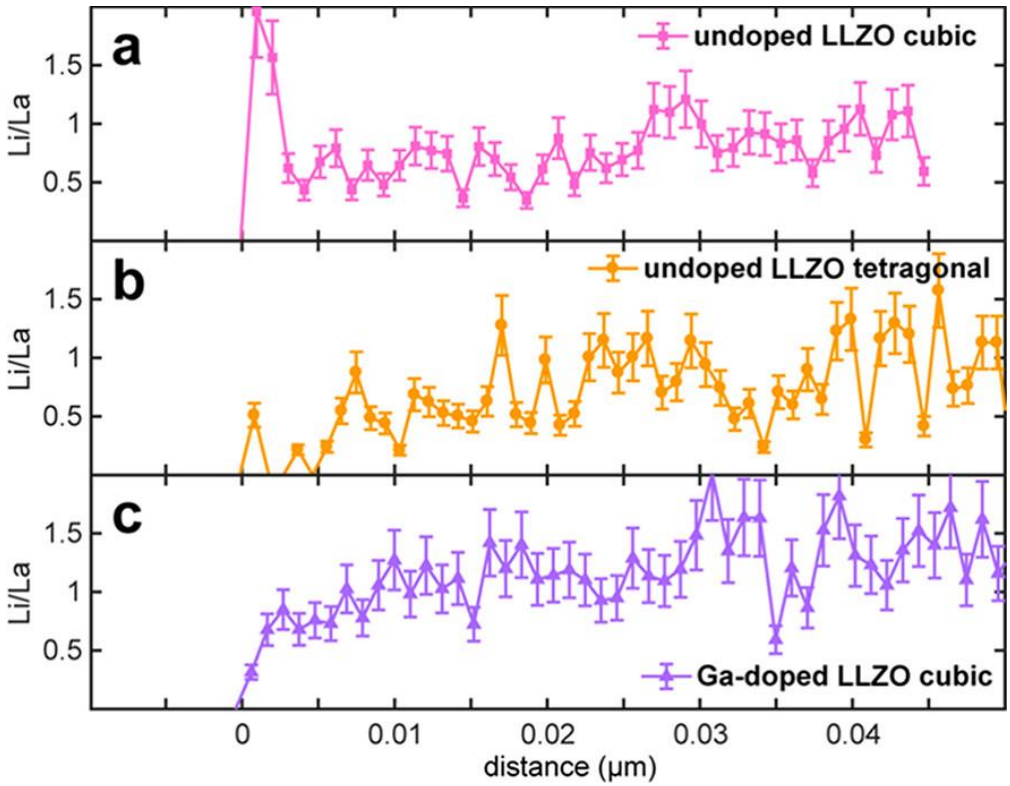

Figure 4. Li/La ratio as calculated from STEM-EELS profiles across the edge of a crystal for (a) undoped cubic-LLZO, (b) undoped tetragonal LLZO, and (c) Ga-doped cubic-LLZO. A relative error of 20% in the ratio, as deriving from the quantification procedure, (46) is considered.

Lithium Loss via Li_2CO_3 Decomposition

As the Li_2CO_3 reactivity and decomposition is key to the available Li stock for c-LLZO formation and its stabilization at room temperature, we performed simulation of CO_2 concentration profiles inside the tubular furnace under N_2 gas flow (from left to right, Figure 5a and Figure S7) of 150 L/h and no flow (see the Supporting Information for more details on the simulation parameters), which is basically CO_2 released as a result of Li_2CO_3 decomposition during 1–2 h of synthesis. We note that at 750 °C the equilibrium concentration of CO_2 would be 0.83% according to the interpolation of the data in Table S1 (based on equilibrium CO_2 pressure at atmospheric pressure as a function of temperature). Figure 5b shows that if the N_2 flow is turned off, the CO_2 concentration around the sample (reactants) reaches a high value of 4% or more after 1 h of reaction. At 750 °C, this is far more than the equilibrium concentration of CO_2, and as a result the decomposition of Li_2CO_3 cannot take place or continue, meaning that the Li_2CO_3 decomposition under this condition would be terminated much earlier than the actual synthesis time (1 h).

Figure 5

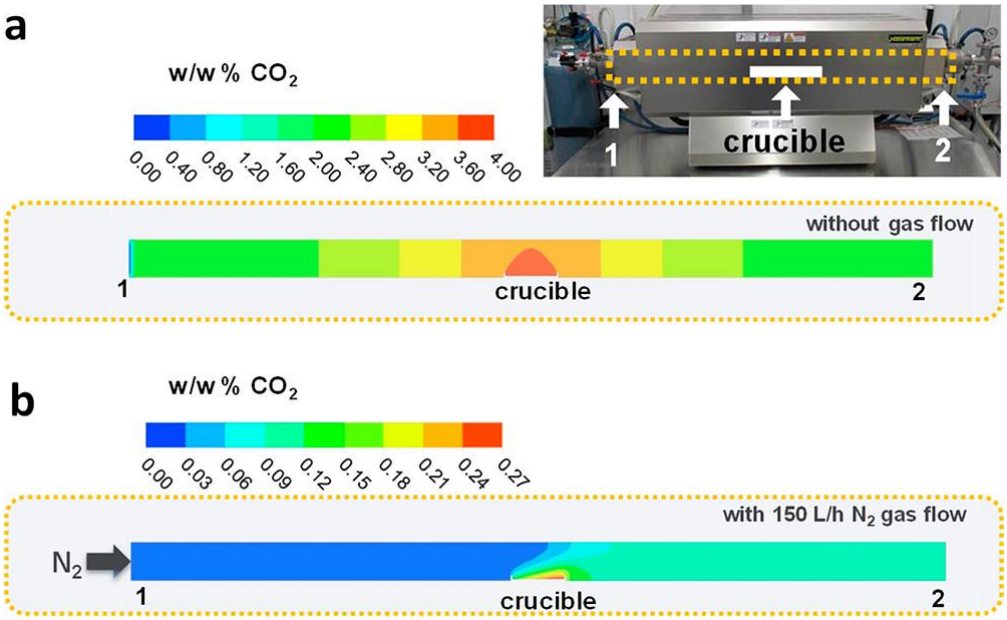

Figure 5. Simulation profile of CO_2 around the crucible in tubular furnace (a) without N_2 gas flow and (b) with N_2 gas flow with inset showing the photo of a tubular furnace.

On the other hand, if the gas flow of N_2 at 150 L/h is turned on, the local CO_2 concentration around the sample becomes far less (0.4%) compared to the synthesis under no N_2 flow, even at 2 h of synthesis (Figure 5b). Therefore, turning off the N_2 gas flow at a low temperature reduces the Li_2CO_3 decomposition rate, which significantly increases the possibility of making more accessible Li (before turning into Li_2O). This Li-rich environment is more favorable to completion of the reaction that yields stoichiometric as well as stabilized cubic-LLZO.

In Figure 6, we summarize our findings deduced from the various experiments conducted. First, $La_2Zr_2O_7$ is formed at ~690 °C, followed by the melting of Li_2CO_3 at 740 °C that is in constant equilibrium between the decomposed products such as Li_2O and gaseous CO_2(Figure 6a). Second, the reaction between the molten Li_2CO_3 and $La_2Zr_2O_7$ typically results in the LLZO formation (Figure 2), where the rate of Li_2CO_3 decomposition is a key parameter that strongly influences the rest of the reaction course in relation to LLZO phase stabilization. A control experiment shows that when a high amount of gallium-doped LLZO powder is annealed without gas flow, amorphous Li_2CO_3 is formed around $La_2Zr_2O_7$ (Figures S8 and S9) due to Li loss. Therefore, the origin of tetragonal LLZO phase formation can be attributed to rapid Li_2CO_3 decomposition (Figure 6b), which is accelerated by the continuous removal of CO_2 during gas flow, causing lithium to be lost as part of Li from Li_2CO_3 is quickly turned into inaccessible Li_2O. This considerably reduces the amount of molten Li_2CO_3 available to react with $La_2Zr_2O_7$ to form LLZO that is still stable cubic phase but only at high temperature. This Li-deficient cubic-LLZO phase is eventually converted into tetragonal LLZO,

for example, upon cooling due to eventual Li loss. On the contrary, without gas flow (Figure 6c) Li_2CO_3 tends to be in the molten state relatively longer by slowing down the decomposition such that it allows for the reaction between Li_2CO_3 and $La_2Zr_2O_7$ until the formation of LLZO is completed under a Li-rich environment.

Figure 6

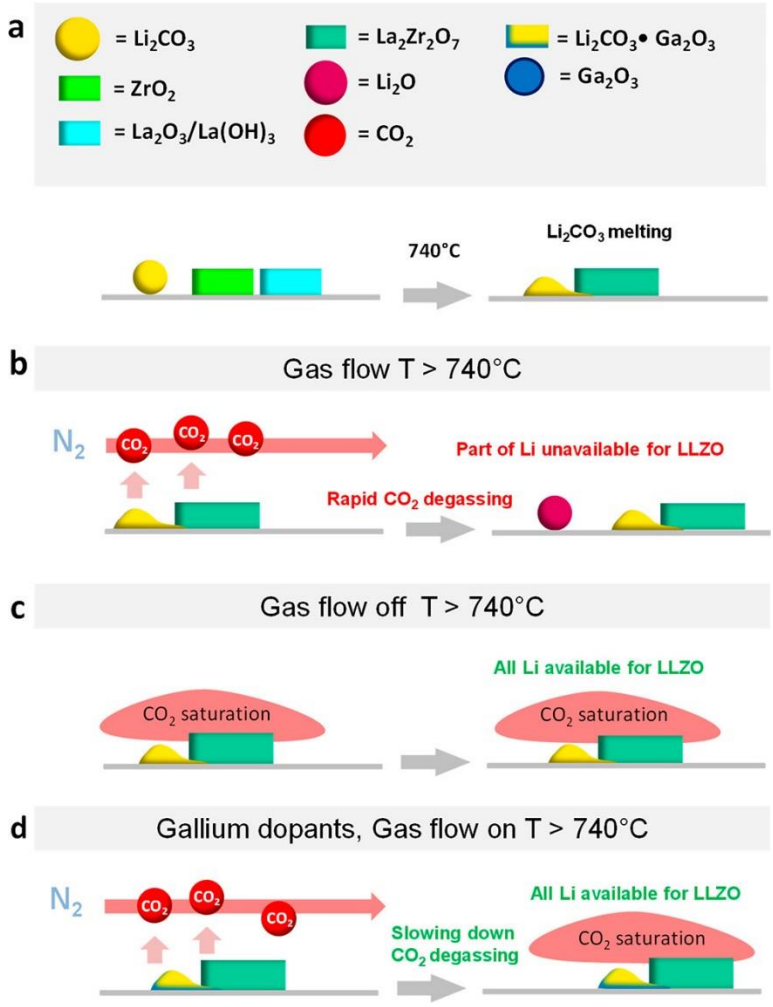

Figure 6. Schematic representing the formation of cubic-LLZO through the control of lithium loss with (a) LLZO precursors at 740 °C, (b) gas flow on, (c) gas flow off, and (d) with the addition of gallium dopant and flow on.

This also applies to the synthesis under gas flow and with gallium as a dopant, producing c-LLZO (Figure 6d), where gallium/lithium gallium oxide can control Li loss because Li_2CO_3 in Li_2CO_3 + Ga_2O_3 decomposes at higher temperature than pure Li_2CO_3, which is in line with thermogravimetric analysis (TGA) as shown in Figure S10. Consequently, the Ga:LLZO precursors react slower between 600 and 800 °C than LLZO precursors without Ga under gas flow (Figure S9). In addition, the reaction products of Li_2CO_3 and Ga_2O_3 appear to delay CO_2 release until the LLZO reaction is completed. When no dopant is supplied, cubic-LLZO (850 °C) is a stable structure but with Li deficiency, and it is then converted to tetragonal LLZO upon cooling down. This conversion is prevented by the homogeneous

distribution of gallium inside the crystals (Figure 3) when a dopant is supplied. Therefore, it turns out that the dopant can also contribute to the preservation of Li during synthesis, favoring a cubic structure that is metastable (without the presence of dopants), and when lithium amount is not stoichiometric, tetragonal LLZO is formed instead of cubic-LLZO. In summary, the synthesis under no gas flow appears to be the best case scenario, where the Li loss at high temperatures is effectively mitigated by slowing down the decomposition of Li_2CO_3. As a result, almost the entire stock of lithium is accessible to the reaction yielding cubic-LLZO phase in a stable form, and during the cooling step, there is no conversion from cubic-LLZO to tetragonal LLZO due to the stabilization through Li retention.

Ionic Conductivity

The Nyquist plots recorded at 20 °C (293 K) for c-LLZO, t-LLZO, and Ga-doped c-LLZO are presented in Figure 7a. Two strongly superimposed semicircles at high and intermediate frequencies are observable, which were fitted with the equivalent circuit model as shown in the Figure 7a inset. The first semicircle (R1-CPE1) is attributable to the LLZO solid electrolyte, while R2-CPE2 is caused by the interface of silver paste used for the measurement. (36) The low-frequency intercept of the semicircle (R1-CPE1) on the Re (Z) axis is the ionic resistance. (47) The ionic conductivity for the three LLZO pellets was calculated by using this resistance and the sample dimensions, and the corresponding activation energies were estimated by solving eq 1 in the Methods section. The Arrhenius plots in the temperature range from 80 °C (353 K) to 20 °C (293 K) for undoped c-LLZO, undoped t-LLZO, and Ga-doped c-LLZO are presented in Figure 7b. The Li ion conductivities of 5.9×10^{-4}, 1.71×10^{-4}, 4.3×10^{-5}, and 8.6×10^{-6} S cm^{-1} at 20 °C (293 K) were obtained for (a) Ga-doped c-LLZO annealed at 1100 °C for 10 h, (b) c-LLZO annealed at 1100 °C for 2 h, (c) c-LLZO annealed at 1100 °C for 10 h, and (d) t-LLZO annealed at 1100 °C for 10 h, respectively. As expected, cubic-LLZO pellets had better ionic conductivity which is in agreement with the total ionic conductivity (lattice and grain boundary) in the range of 1×10^{-4} and 1×10^{-3} S cm^{-1} at room temperature previously reported for cubic-LLZO (48,49) and 10^{-7}–10^{-6} S cm^{-1} for the tetragonal structure. (50,51) These ionic conductivity values also reflect the results from *in situ* XRD patterns in Figure 2 that during an SSR at high temperatures Li loss/retention is a key to LLZO phase stabilization, which is most likely mediated by Li_2CO_3 decomposition kinetics (Figure 6). From the Arrhenius plots in Figure 7b, the calculated activation energy for charge transport in the different LLZO pellets was in the range 0.41–0.48 eV. These values are in agreement with previous reports on ceramics-based electrolytes. (52,53)

Figure 7

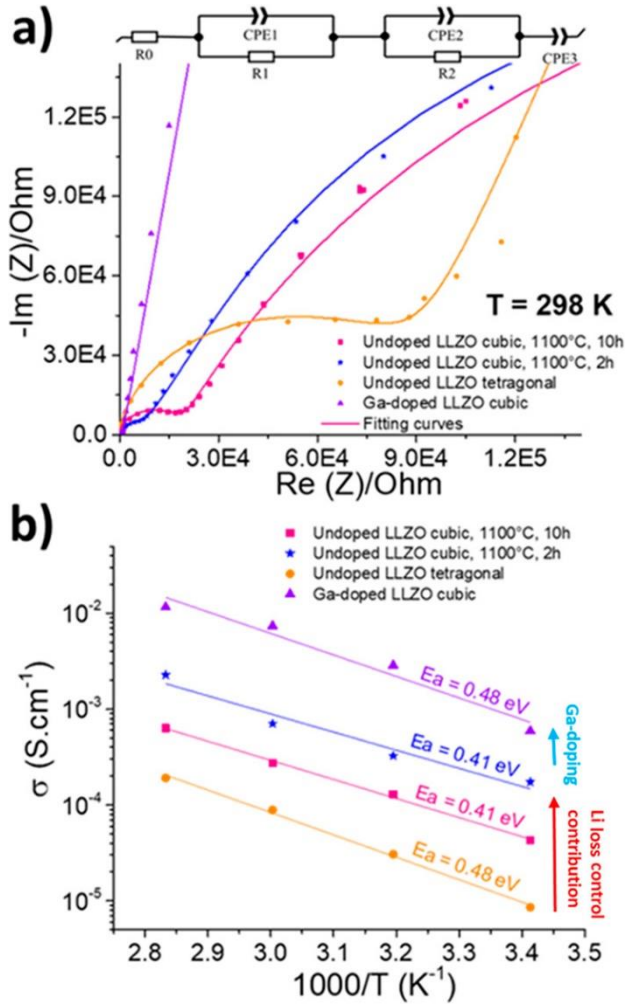

Figure 7. (a) Electrochemical impedance spectroscopy data at 25 °C. (b) Arrhenius plots for undoped LLZO cubic annealed at 1100 °C for 2 and 10 h, undoped LLZO tetragonal annealed at 1100 °C for 10 h, and Ga-doped LLZO annealed at 1100 °C for 10 h (R^2 factor linear for fit—undoped LLZO cubic, 1100 °C, 10 h, R^2 = 0.997; undoped LLZO cubic, 1100 °C, 2 h, R^2 = 0.996; undoped LLZO tetragonal, R^2 = 0.941; Ga-doped LLZO cubic, R^2 = 0.955).

Moreover, it can be noted that c-LLZO annealed at 1100 °C for 2 h had a better ionic conductivity than the same sample annealed at 1100 °C for 10 h (Figure 6), as the undoped c-LLZO is metastable and is dependent on the sintering time. During the densification process, undoped cubic-LLZO annealed at 1100 °C becomes tetragonal in the presence of gas flow and form La_2Zr_2O under no gas. Because of this reason, pellets sintered for shorter annealing time may show higher conductivities. Figure S11 shows an *in situ* XRD sintering, where gas flow during the densification step was able to convert cubic-LLZO into tetragonal LLZO, indicating that undoped cubic-LLZO is metastable. And after sintering, a $La_2Zr_2O_7$ impurity (present before sintering) had disappeared, suggesting a possible lithium migration reaction between c-LLZO and $La_2Zr_2O_7$. In the case of synthesis under no gas flow during the sintering process, cubic-LLZO was preserved, while the

amount of $La_2Zr_2O_7$ increased, probably due to lithium loss. Therefore, on the basis of these experiments, we conclude that the role of gallium dopants is to control lithium loss (in addition to substituting for Li in Li sites) during both the synthesis and densification steps.

Conclusion

We have shown that c-LLZO with phase stability and higher ionic conductivity than standard t-LLZO can be directly processed by simply carrying out the synthesis under no gas flow (N_2) and without needing dopants. This is achieved by effectively controlling Li loss at high temperatures as the decomposition of Li carbonate precursor leads to either accessible Li for the formation of LLZO stable cubic phase or inaccessible Li_2O leading to lithium-deficient LLZO unstable phase (tetragonal) or off-stoichiometric LLZO or pyrochlore ($La_2Zr_2O_7$). We have also shown that the addition of gallium dopant can contribute to control this Li loss as lithium carbonate decomposition is slowed down leading to more available Li^+ ions for c-LLZO formation, indicating that in the conventional solid-state synthesis routes of LLZO that are supplemented by extra dopants an additional role of dopants is to retain accessible Li. Our structural, simulation, and microscopic data shed new light on LLZO reaction and phase transformation and on the various stages of LLZO formation, while identifying a control mechanism for Li loss during solid-state synthesis. Thus, our findings can catalyze new developments in the design and solid-state manufacturing of garnet-type solid electrolytes with high phase stability and ionic conductivity.

Acknowledgments

The work was funded by Hydro-Quebec. The authors thank Dr. Ashok Vijh, Dr. Alexis Perea and Dr. Yuesheng Wang of Hydro-Quebec for useful comments. C.G. acknowledges the Royal Society for an URF.

References

1. Cheng, X.; Zhang, R.; Zhao, C.; Zhang, Q. Toward Safe Lithium Metal Anode in Rechargeable Batteries: A Review. *Chem. Rev.* **2017**, *117*, 10403– 10473, DOI: 10.1021/acs.chemrev.7b00115
2. Guo, Y.; Li, H.; Zhai, T. Reviving Lithium-Metal Anodes for Next-Generation High-Energy Batteries. *Adv. Mater.* **2017**, *29*, 1700007, DOI: 10.1002/adma.201700007
3. Liu, J.; Bao, Z.; Cui, Y.; Dufek, E. J.; Goodenough, J. B.; Khalifah, P.; Li, Q.; Liaw, B. Y.; Liu, P.; Manthiram, A.; Meng, Y. S.; Subramanian, V. R.; Toney, M. F.; Viswanathan, V. V.; Whittingham, M. S.; Xiao, J.; Xu, W.; Yang, J.; Yang, X.-Q.; Zhang, J.-G. Pathways for practical high-energy long-cycling lithium metal batteries. *Nat. Energy* **2019**, *4*, 180– 186, DOI: 10.1038/s41560-019-0338-x

4. Khurana, R.; Schaefer, J. L.; Archer, L. A.; Coates, G. W. Suppression of Lithium Dendrite Growth Using Cross-Linked Polyethylene/Poly(ethylene oxide) Electrolytes: A New Approach for Practical Lithium-Metal Polymer Batteries. *J. Am. Chem. Soc.* **2014**, *136*, 7395– 7402, DOI: 10.1021/ja502133j
5. Zhao, Q.; Liu, X.; Stalin, S.; Khan, K.; Archer, L. A. Solid-state polymer electrolytes with in-built fast itnerfacial transport for secondary lithium batteries. *Nat. Energy* **2019**, *4*, 365– 373, DOI: 10.1038/s41560-019-0349-7
6. Zhu, Y.; Connell, J. G.; Tepavcevic, S.; Zapol, P.; Garcia-Mendez, R.; Taylor, N. J.; Sakamoto, J.; Ingram, B. J.; Curtiss, L. A.; Freeland, J. W.; Fong, D. D.; Markovic, N. M. Dopant-Dependent Stability of Garnet Solid Electrolyte Interfaces with Lithium Metal. *Adv. Energy Mater.* **2019**, *9*, 1803440, DOI: 10.1002/aenm.201803440
7. Westover, A. S.; Dudney, N. J.; Sacci, R. L.; Kalnaus, S. Deposition and Confinement of Li Metal along an Artificial Lipon–Lipon Interface. *ACS Energy Lett.* **2019**, *4*, 651, DOI: 10.1021/acsenergylett.8b02542
8. Zhang, J.; Zhao, N.; Zhang, M.; Li, Y.; Chu, P. K.; Guo, X.; Di, Z.; Wang, X.; Li, H. Flexible and ion-conducting membrane electrolytes for solid-state lithium batteries : Dispersion of garnet nanoparticles in insulating polyethylene oxide. *Nano Energy* **2016**, *28*, 447– 454, DOI: 10.1016/j.nanoen.2016.09.002
9. Wan, Z.; Lei, D.; Yang, W.; Liu, C.; Shi, K.; Hao, X.; Shen, L.; Lv, W.; Li, B.; Yang, Q.-H.; Kang, F.; He, Y.-B. Low Resistance – Integrated All-Solid-State Battery Achieved by Li7La3Zr 2O12 Nanowire Upgrading Polyethylene Oxide (PEO) Composite Electrolyte and PEO Cathode Binder. *Adv. Funct. Mater.* **2019**, *29*, 1970006, DOI: 10.1002/adfm.201970006
10. Chen, L.; Li, Y.; Li, S. P.; Fan, L. Z.; Nan, C. W.; Goodenough, J. B. PEO/garnet composite electrolytes for solid-state lithium batteries: From ‘ ceramic-in-polymer ’ to ‘ polymer-in-ceramic ’. *Nano Energy* **2018**, *46*, 176– 184, DOI: 10.1016/j.nanoen.2017.12.037
11. Zheng, J.; Dang, H.; Feng, X.; Chien, P. H.; Hu, Y. Y. Li-ion transport in a representative ceramic-polymer-plasticizer composite electrolyte: Li7La3Zr2O12-polyethylene oxide-tetraethylene glycol dimethyl ether. *J. Mater. Chem. A* **2017**, *5*, 18457– 18463, DOI: 10.1039/C7TA05832B
12. Kanno, R.; Murayama, M. Lithium Ionic Conductor Thio-LISICON. *J. Electrochem. Soc.* **2001**, *148*, 742– 746, DOI: 10.1149/1.1379028
13. Wu, F.; Fitzhugh, W.; Ye, L.; Ning, J.; Li, X. Advanced sulfide solid electrolyte by core-shell structural design. *Nat. Commun.* **2018**, *9*, 1– 11, DOI: 10.1038/s41467-018-06123-2
14. Hartmann, P.; Leichtweiss, T.; Busche, M. R.; Schneider, M.; Reich, M.; Sann, J.; Adelhelm, P.; Janek, J. Degradation of NASICON-Type Materials in Contact with Lithium Metal:

Formation of Mixed Conducting Interphases (MCI) on Solid Electrolytes. *J. Phys. Chem. C* **2013**, *117*, 21064– 21074, DOI: 10.1021/jp4051275

15. Zhang, W.; Richter, F.; Culver, S. P.; Leichtweiß, T.; Lozano, J. G.; Dietrich, C.; Bruce, P. G.; Zeier, W. G.; Janek, J. Degradation Mechanisms at the Li10GeP2S12 /LiCoO2 Cathode Interface in an All-Solid-State Lithium-Ion Battery. *ACS Appl. Mater. Interfaces* **2018**, *10*, 22226– 22236, DOI: 10.1021/acsami.8b05132
16. Emly, A.; Kioupakis, E.; Van der Ven, A. Phase Stability and Transport Mechanisms in Antiperovskite Li3OCl and Li3OBr Superionic Conductors. *Chem. Mater.* **2013**, *25*, 4663– 4670, DOI: 10.1021/cm4016222
17. Braga, M. H.; Murchison, A. J.; Ferreira, J. A.; Singh, P.; Goodenough, J. B. Glass-amorphous alkali-ion solid electrolytes and their performance in symmetrical cells. *Energy Environ. Sci.* **2016**, *9*, 948– 954, DOI: 10.1039/C5EE02924D
18. Steingart, D. A.; Viswanathan, V. Comment on Alternative strategy for a safe rechargeable battery. *Energy Environ. Sci.* **2018**, *11*, 221– 222, DOI: 10.1039/C7EE01318C
19. Hanghofer, I.; Redhammer, G. J.; Rohde, S.; Hanzu, I.; Senyshyn, A.; Wilkening, H. M. R.; Rettenwander, D. Untangling the Structure and Dynamics of Lithium-Rich Anti-Perovskites Envisaged as Solid Electrolytes for Batteries. *Chem. Mater.* **2018**, *30*, 8134– 8144, DOI: 10.1021/acs.chemmater.8b02568
20. Safanama, D.; Damiano, D.; Prasada, R.; Adams, S. Lithium conducting solid electrolyte Li1+xAlxGe2–x(PO4)3 membrane for aqueous lithium air battery. *Solid State Ionics* **2014**, *262*, 211– 215, DOI: 10.1016/j.ssi.2013.11.031
21. Soman, S.; Iwai, Y.; Kawamura, J.; Kulkarni, A. Crystalline phase content and ionic conductivity correlation in LATP glass – ceramic. *J. Solid State Electrochem.* **2012**, *16*, 1761– 1766, DOI: 10.1007/s10008-011-1592-4
22. Chung, H.; Kang, B. Mechanical and Thermal Failure Induced by Contact between a Li1.5Al0.5Ge1.5(PO4)3 Solid Electrolyte and Li Metal in an All Solid-State Li Cell. *Chem. Mater.* **2017**, *29*, 8611– 8619, DOI: 10.1021/acs.chemmater.7b02301
23. Duan, J.; Wu, W.; Nolan, A. M.; Wang, T.; Wen, J.; Hu, C.; Mo, Y.; Luo, W.; Huang, Y. Lithium–Graphite Paste: An Interface Compatible Anode for Solid-State Batteries. *Adv. Mater.* **2019**, *31*, 1807243, DOI: 10.1002/adma.201807243
24. Geiger, C. A.; Alekseev, E.; Lazic, B.; Fisch, M.; Armbruster, T.; Langner, R.; Fechtelkord, M.; Kim, N.; Pettke, T.; Weppner, W. Crystal Chemistry and Stability of 'Li7La3Zr2O12' Garnet : A Fast Lithium-Ion Conductor. *Inorg. Chem.* **2011**, *50*, 1089– 1097, DOI: 10.1021/ic101914e

25. Rettenwander, D.; Geiger, C. A.; Amthauer, G. Synthesis and Crystal Chemistry of the Fast Li-Ion Conductor Li7La3Zr2O12 Doped with Fe. *Inorg. Chem.* **2013**, *52*, 8005– 8009, DOI: 10.1021/ic400589u
26. El Shinawi, H.; Janek, J. Stabilization of cubic lithium-stuffed garnets of the type 'Li7La3Zr2O12' by addition of gallium. *J. Power Sources* **2013**, *225*, 13– 19, DOI: 10.1016/j.jpowsour.2012.09.111
27. Xiang, X.; Chen, F.; Shen, Q.; Zhang, L.; Chen, C. Effect of the lithium ion concentration on the lithium ion conductivity of Ga-doped LLZO. *Mater. Res. Express* **2019**, *6*, 085546, DOI: 10.1088/2053-1591/ab2799
28. Rettenwander, D.; Langer, J.; Schmidt, W.; Arrer, C.; Harris, K. J.; Terskikh, V.; Goward, G. R.; Wilkening, M.; Amthauer, G. Site occupation of Ga and Al in stabilized cubic Li7–3(x + y)GaxAlyLa3Zr2O12 garnets as deduced from 27Al and 71Ga MAS NMR at ultrahigh magnetic fields. *Chem. Mater.* **2015**, *27*, 3135– 3142, DOI: 10.1021/acs.chemmater.5b00684
29. Xia, W.; Xu, B.; Duan, H.; Guo, Y.; Kang, H.; Li, H.; Liu, H. Ionic Conductivity and Air Stability of Al-Doped Li7La3Zr2O12 Sintered in Alumina and Pt Crucibles. *ACS Appl. Mater. Interfaces* **2016**, *8*, 5335– 5342, DOI: 10.1021/acsami.5b12186
30. Rangasamy, E.; Wolfenstine, J.; Sakamoto, J. The role of Al and Li concentration on the formation of cubic garnet solid electrolyte of nominal composition Li7La3Zr2O12. *Solid State Ionics* **2012**, *206*, 28– 32, DOI: 10.1016/j.ssi.2011.10.022
31. García Daza, F. A.; Bonilla, M. R.; Llordés, A.; Carrasco, J.; Akhmatskaya, E. Atomistic Insight into Ion Transport and Conductivity in Ga/Al-Substituted Li 7 La 3 Zr 2 O 12 Solid Electrolytes. *ACS Appl. Mater. Interfaces* **2019**, *11*, 753– 765, DOI: 10.1021/acsami.8b17217
32. Thompson, T.; Wolfenstine, J.; Allen, J. L.; Johannes, M.; Huq, A.; David, I. N.; Sakamoto, J. Tetragonal vs. cubic phase stability in Al-free Ta doped Li 7La3Zr2O12 (LLZO). *J. Mater. Chem. A* **2014**, *2*, 13431– 13436, DOI: 10.1039/C4TA02099E
33. Rosero-Navarro, N. C.; Yamashita, T.; Miura, A.; Higuchi, M.; Tadanaga, K. Preparation of Li7La3(Zr2-xNbx)O12 (x = 0–1.5) and Li3BO3/LiBO2 composites at low temperatures using a sol – gel process. *Solid State Ionics* **2016**, *285*, 6– 12, DOI: 10.1016/j.ssi.2015.06.015
34. Meier, K.; Laino, T.; Curioni, A. Solid-State Electrolytes: Revealing the Mechanisms of Li-Ion Conduction in Tetragonal and Cubic LLZO by First-Principles Calculations. *J. Phys. Chem. C* **2014**, *118*, 6668– 6679, DOI: 10.1021/jp5002463
35. Kubicek, M.; Wachter-Welzl, A.; Rettenwander, D.; Wagner, R.; Berendts, S.; Uecker, R.; Amthauer, G.; Hutter, H.; Fleig, J. Oxygen Vacancies in Fast Lithium-Ion Conducting Garnets. *Chem. Mater.* **2017**, *29*, 7189– 7196, DOI: 10.1021/acs.chemmater.7b01281

36. Xie, H.; Li, Y.; Goodenough, J. B. Low-temperature synthesis of Li7La3Zr2O12 with cubic garnet-type structure. *Mater. Res. Bull.* **2012**, *47*, 1229– 1232, DOI: 10.1016/j.materresbull.2012.01.027
37. Larraz, G.; Orera, A.; Sanjuán, M. L. Cubic phases of garnet-type Li7La3Zr2O12: The role of hydration. *J. Mater. Chem. A* **2013**, *1*, 11419– 11428, DOI: 10.1039/c3ta11996c
38. Yang, T.; Gordon, Z. D.; Li, Y.; Chan, C. K. Nanostructured Garnet-Type Solid Electrolytes for Lithium Batteries: Electrospinning Synthesis of Li7La3Zr2O12 Nanowires and Particle Size-Dependent Phase Transformation. *J. Phys. Chem. C* **2015**, *119*, 14947– 14953, DOI: 10.1021/acs.jpcc.5b03589
39. Weller, J. M.; Whetten, J. A.; Chan, C. K. Synthesis of Fine Cubic Li7La3Zr2O12 Powders in Molten LiCl-KCl Eutectic and Facile Densification by Reversal of Li + /H + Exchange. *ACS Appl. Energy Mater.* **2018**, *1*, 552– 560, DOI: 10.1021/acsaem.7b00133
40. Bernal, S.; Botana, F.J.; Garcia, R.; Rodriguez-Izquierdo, J.M. Thermal evolution of a sample of La2O3 exposed to the atmosphere. *Thermochim. Acta* **1983**, *66*, 139– 145, DOI: 10.1016/0040-6031(93)85026-6
41. Deviannapoorani, C.; Ramakumar, S.; Janani, N.; Murugan, R. Synthesis of lithium garnets from La2Zr2O7 pyrochlore. *Solid State Ionics* **2015**, *283*, 123– 130, DOI: 10.1016/j.ssi.2015.10.006
42. Chen, Y.; Rangasamy, E.; Dela Cruz, C. R.; Liang, C.; An, K. A Study of Suppressed Formation of Low-Conductive Phases in Doped Li7La3Zr2O12 Garnets by in-situ Neutron Diffraction. *J. Mater. Chem. A* **2015**, *3*, 22868– 22876, DOI: 10.1039/C5TA04902D
43. Rao, R. P.; Gu, W. Y.; Sharma, N.; Peterson, V. K.; Avdeev, M.; Adams, S. In Situ Neutron Diffraction Monitoring of Li 7 La 3 Zr 2 O 12 Formation: Toward a Rational Synthesis of Garnet Solid Electrolytes. *Chem. Mater.* **2015**, *27*, 2903– 2910, DOI: 10.1021/acs.chemmater.5b00149
44. Kim, J.; Lee, H. Thermal and Carbothermic Decomposition of Na2CO3 and Li2CO3. *Metall. Mater. Trans. B* **2001**, *32*, 17– 24, DOI: 10.1007/s11663-001-0003-0
45. Huang, X.; Shen, C.; Rui, K.; Jin, J.; Wu, M.; Wu, X.; Wen, Z. Influence of La2Zr2O7 Additive on Densification and Li + Conductivity for Ta-Doped Li7La3Zr2O12 Garnet. *JOM* **2016**, *68*, 2593– 2600, DOI: 10.1007/s11837-016-2065-0
46. Bertoni, G.; Verbeeck, J. Accuracy and precision in model based EELS quantification. *Ultramicroscopy* **2008**, *108*, 782– 790, DOI: 10.1016/j.ultramic.2008.01.004
47. Huggins, R. A. Simple Method to Determine Electronic and Ionic Components of the Conductivity in Mixed Conductors A Review. *Ionics* **2002**, *8*, 300– 313, DOI: 10.1007/BF02376083

48. Shimonishi, Y.; Toda, A.; Zhang, T.; Hirano, A.; Imanishi, N.; Yamamoto, O.; Takeda, Y. Synthesis of garnet-type Li7–x La3Zr2O12–1/2x and its stability in aqueous solutions. *Solid State Ionics* **2011**, *183*, 48– 53, DOI: 10.1016/j.ssi.2010.12.010
49. Kumazaki, S.; Iriyama, Y.; Kim, K. H.; Murugan, R.; Tanabe, K.; Yamamoto, K.; Hirayama, T.; Ogumi, Z. High lithium ion conductive Li7La3Zr2O12 by inclusion of both Al and Si. *Electrochem. Commun.* **2011**, *13*, 509– 512, DOI: 10.1016/j.elecom.2011.02.035
50. Awaka, J.; Kijima, N.; Hayakawa, H.; Akimoto, J. Synthesis and structure analysis of tetragonal Li7La3Zr2O12 with the garnet-related type structure. *J. Solid State Chem.* **2009**, *182*, 2046– 2052, DOI: 10.1016/j.jssc.2009.05.020
51. Il'ina, E.A.; Andreev, O.L.; Antonov, B.D.; Batalov, N.N. Morphology and transport properties of the solid electrolyte Li7La3Zr2O12 prepared by the solid-state and citrate – nitrate methods. *J. Power Sources* **2012**, *201*, 169– 173, DOI: 10.1016/j.jpowsour.2011.10.108
52. Loho, C.; Djenadic, R.; Bruns, M.; Clemens, O.; Hahn, H. Garnet-Type Li7La3Zr2O12 Solid Electrolyte Thin Films Grown by CO2-Laser Assisted CVD for All-Solid-State Batteries. *J. Electrochem. Soc.* **2017**, *164*, A6131, DOI: 10.1149/2.0201701jes
53. Buschmann, H.; Dölle, J.; Berendts, S.; Kuhn, A.; Bottke, P.; Wilkening, M.; Heitjans, P.; Senyshyn, A.; Ehrenberg, H.; Lotnyk, A.; Duppel, V.; Kienle, L.; Janek, J. Structure and dynamics of the fast lithium ion conductor "Li7La3Zr2O12". *Phys. Chem. Chem. Phys.* **2011**, *13*, 19378– 19392, DOI: 10.1039/c1cp22108f